Morphological Cell Profiling of SARS-CoV-2 Infection Identifies Drug Repurposing Candidates for COVID-19

Carmen Mirabelli[1,*], Jesse W. Wotring[2,*], Charles J. Zhang[2,†], Sean M. McCarty[2,†], Reid Fursmidt[3,4,†], Tristan Frum[5,] Namrata S. Kadambi[3], Anya T. Amin[3], Teresa R. O'Meara[1], Carla D. Pretto[1], Jason R. Spence[3,5], Jessie Huang[6,7], Konstantinos D. Alysandratos[6,7], Darrell N. Kotton[6,7], Samuel K. Handelman[3,4], Christiane E. Wobus[1], Kevin J. Weatherwax[4,8,9], George A. Mashour[4,8,10], Matthew J. O'Meara[11], Jonathan Z. Sexton[2,3,4,8]

[1]Department of Microbiology and Immunology, University of Michigan Medical School, Ann Arbor, MI, 48109, USA
[2]Department of Medicinal Chemistry, College of Pharmacy, University of Michigan, Ann Arbor, MI, 48109, USA
[3]Department of Internal Medicine, Gastroenterology, Michigan Medicine at the University of Michigan, Ann Arbor, MI, 48109, USA
[4]U-M Center for Drug Repurposing, University of Michigan, Ann Arbor, MI, 48109, USA
[5]Department of Cell and Developmental Biology, University of Michigan, Ann Arbor, MI, 48109, USA
[6]Center for Regenerative Medicine of Boston University and Boston Medical Center, Boston, MA, 02118, USA
[7]The Pulmonary Center and Department of Medicine, Boston University School of Medicine, Boston, MA, 02118, USA
[8]Michigan Institute for Clinical and Health Research (MICHR), University of Michigan, Ann Arbor, MI, 48109, USA
[9]College of Pharmacy, University of Michigan, Ann Arbor, MI 48109, USA
[10]Department of Anesthesiology, Michigan Medicine at the University of Michigan, Ann Arbor, MI, 48109, USA
[11]Department of Computational Medicine and Bioinformatics, University of Michigan, Ann Arbor, MI, 48109, USA

[*]These authors contributed equally to this work.
[†]These authors contributed equally to this work.

Abbreviations:

MOI: multiplicity of infection
UMAP: uniform manifold approximation and projection
COVID-19: Coronavirus Disease-2019
MOA: mechanism of action
ROI: region of interest
iAEC2: induced pluripotent stem cell (iPSC)-derived alveolar epithelial type 2 cells
HCQ: hydroxychloroquine

Conflicts of interest

The authors declare no conflicts of interest.

ABSTRACT

The global spread of the severe acute respiratory syndrome coronavirus 2 (SARS-CoV-2), and the associated disease COVID-19, requires therapeutic interventions that can be rapidly translated to clinical care. Unfortunately, traditional drug discovery methods have a >90% failure rate and can take 10-15 years from target identification to clinical use. In contrast, drug repurposing can significantly accelerate translation. We developed a quantitative high-throughput screen to identify efficacious single agents and combination therapies against SARS-CoV-2. Quantitative high-content morphological profiling was coupled with an AI-based machine learning strategy to classify features of cells for infection and stress. This assay detected multiple antiviral mechanisms of action (MOA), including inhibition of viral entry, propagation, and modulation of host cellular responses. From a library of 1,425 FDA-approved compounds and clinical candidates, we identified 16 dose-responsive compounds with antiviral effects. In particular, we discovered that lactoferrin is an effective inhibitor of SARS-CoV-2 infection with an IC_{50} of 308 nM and that it potentiates the efficacy of both remdesivir and hydroxychloroquine. Lactoferrin also stimulates an antiviral host cell response and retains inhibitory activity in iPSC-derived alveolar epithelial cells, a model for the primary site of infection. Given its safety profile in humans, these data suggest that lactoferrin is a readily translatable therapeutic adjunct for COVID-19. Additionally, several commonly prescribed drugs were found to exacerbate viral infection and warrant clinical investigation. We conclude that morphological profiling for drug repurposing is an effective strategy for the selection and optimization of drugs and drug combinations as viable therapeutic options for COVID-19 pandemic and other emerging infectious diseases.

MAIN

SARS-CoV-2 is an enveloped, positive-sense, single-stranded RNA betacoronavirus that emerged in Wuhan, China in November 2019 and rapidly developed into a global pandemic. The associated disease, COVID-19, has an array of symptoms, ranging from flu-like illness and gastrointestinal distress[1,2] to acute respiratory distress syndrome, heart arrhythmias, strokes, and death[3,4]. Drug repurposing has played an important role in the search for COVID-19 therapies. Recently, the FDA issued emergency approval of remdesivir, a nucleoside inhibitor prodrug developed for Ebola virus treatment[5], and hydroxychloroquine, an aminoquinoline derivative first developed in the 1940s for the treatment of malaria, for patients with severe COVID-19. However, there are no established prophylactic strategies or direct antiviral treatments available to limit SARS-CoV-2 infections and to prevent/cure the associated disease COVID-19.

Repurposing of FDA-approved drugs is a promising strategy for identifying rapidly deployable treatments for COVID-19. Benefits of repurposing include known safety profiles, robust supply chains, and a short time-frame necessary for development[6]. Additionally, approved drugs serve as chemical probes to understand the biology of viral infection and can make new associations between COVID-19 and molecular targets/pathways that influence pathogenesis of the disease. A complementary approach to standard *in vitro* antiviral assays is high-content imaging-based morphological cell profiling. Using morphological cell profiling, it is possible to identify pathways and novel biology underlying infection, thus allowing for targeted screening around a particular biological process or targeting of host processes that limit viral infection. This enables the identification of multiple anti-viral mechanisms, allowing for the rational design of drug combinations or, conversely, revealing drugs that exacerbate infectivity or are associated with cytotoxicity.

Here, we developed a pipeline for quantitative high-throughput image-based screening of SARS-CoV-2 infection. We leveraged machine learning approaches to create an assay metric that accurately and robustly identifies features that predict antiviral efficacy and mechanism of action (MOA). We identified several FDA-approved drugs and clinical candidates with unique antiviral activity. We further demonstrated that lactoferrin inhibits viral entry and replication, enhances antiviral host cell response, and potentiates the effects of remdesivir and hydroxychloroquine. Furthermore, we identified currently prescribed drugs that exacerbate viral infectivity. As a confirmatory step, efficacy of lead drugs was validated in a highly physiologically relevant organotypic and biomimetic human model system for bronchial epithelium. Collectively, we present evidence that morphological profiling can robustly identify new potential therapeutics against SARS-CoV-2 infection as well as drugs that potentially worsen COVID-19 outcomes.

Morphological profiling reveals unique features associated with SARS-CoV-2 infection

To determine the optimal cell line and appropriate endpoint for antiviral drug screening, we assessed SARS-CoV-2 infectivity in previously reported permissive cell lines: Vero E6, Caco-2, and Huh7[7]. Viral growth kinetics at a multiplicity of infection (MOI) of 0.2 revealed that Vero E6, Caco-2, and Huh7 cells supported viral infection, with peak viral titers at 48 hours post infection (hrs p.i.) (Supplementary Figure 1a/b). Although the viral load was higher in Vero E6 cells, Huh7 were selected for our morphological drug screen as a human cell line that expresses both ACE2 and TMPRSS2, which are the primary entry factors for SARS-CoV-2[8]. Infection was detectable in Huh7 cells at an MOI as low as 0.004 at 48 hrs p.i. (Supplementary Figure 1c), which highlights the high sensitivity of image-based screening. To identify compounds that inhibit or exacerbate infection, we selected an MOI of 0.2, leading to a baseline infectivity rate of 20%.

Morphological cell profiling was enabled through multiplexed staining and automated high-content fluorescence microscopy. Our multiplexed dye set included markers for SARS-CoV-2 nucleocapsid protein (NP), nuclei (Hoechst 33342), neutral lipids (HCS LipidTox Green), and cell boundaries (HCS CellMask Orange). These fluorescent probes were chosen to capture a wide variety of cellular features relevant to viral infectivity, including nuclear morphology, nuclear texture, cytoplasmic and cytoskeletal features, and indicators of cell health. From initial profiling, we observed three prominent morphological features associated with SARS-CoV-2 infection: the formation of syncytia, increased nucleoli count (Supplementary Figure 1d), and cytoplasmic protrusions (Figure 1). These features, which are key indicators of SARS-CoV-2 infection in Huh7, were used to generate our machine learning pipeline for antiviral drug discovery.

Machine learning identifies FDA-approved molecules with antiviral activity against SARS-CoV-2

To identify compounds with antiviral activity against SARS-CoV-2, we screened a library of 1,425 FDA-approved compounds and rationally included clinical candidates (Supplementary File 1) in quantitative high-throughput screening (qHTS) at five concentrations (50 nM, 250 nM, 500 nM, 1000 nM and 2000 nM) in Huh7 cells. Compounds were assessed for their antiviral activity using a CellProfiler-based image analysis pipeline and a random forest classification algorithm to identify infected cells and quantify their morphological characteristics (Figure 2a). The random forest classifier leveraged 660 unique cellular features including measurements of intensity, texture and radial distribution for each fluorescent channel (nuclei, cytoplasm, lipid, virus). From the qHTS, we identified 132 drugs as active with consistent decreases in viral infectivity in at least three of the tested concentrations as well as minimal cytotoxicity.

In confirmatory screening, 10-point, two-fold dilution dose-response experiments were performed in triplicate on the 132 qHTS hits, with validation of dose-responsive efficacy for 16 compounds below 1 μM potency (Supplementary Table 1 and Figure 2b). These hits include eleven that are novel *in vitro* observations (bosutinib, domperidone, entecavir, fedratinib, ipratropium bromide, lacoferrin, lomitapide, metoclopramide, S1RA, thioguanine, and Z-FA-FMK), and six that have been previously identified to have antiviral activity (amiodarone, verapamil, gilteritinib, clofazimine[9,10], niclosamide[11], and remdesivir). Amiodarone, gilterinib, lomitapide, thioguanidine and Z-FA-FMK retained activity in a traditional CPE-based antiviral assay in Vero E6 (Supplementary Table 1). In addition to antiviral drug hits, we also identified several compounds that appear to exacerbate SARS-CoV-2 infection, including trametinib, binimetinib and cobimetinib -potent MEK inhibitors used to treat metastatic melanoma- and the Parkinson's disease drugs carbidopa, methyldopa and levodopa (Supplementary Figure 2).

Cell level feature clustering reveals potential mechanisms of action for lead compounds

In contrast to standard single-endpoint *in vitro* assays, morphological cell profiling allows for the efficient visualization and quantitation of biological characteristics of viral infection and cytotoxicity. To assist with mechanistic determination, 379 representative cellular features were dimensionality reduced via the non-linear uniform manifold approximation and projection (UMAP) to embed for 1.96 million cells into 2-dimensions to plot clusters of cells based on their distinct morphological features[12]. Then we re-embed 18.9 million cells from 15 plates to observe the perturbation of feature distributions through a range of drug concentrations relative to negative and positive controls (Figure 2, Supplementary Figure 3b).

In the UMAP embedding, we identified 15 regions of interest (ROI) with high cell density (Figure 3b). A broad density region (ROIs 10,15) contained 8.4 million uninfected cells with satellite populations having characteristic morphologies including 0.59 million undergoing cell division (ROI 6) and 1.09 million accumulating of lipids towards the periphery of the cell (ROI 12). A large disconnected region (ROIs 1-4) contained 85 thousand isolated infected cells (ROI 4), 0.43 million infected cells in syncytia (ROI 3), and 1.3 million cells adjacent to infected cells (ROIs 1,2) (Figure 3c). Pseudotime of the viral infection progression can be inferred through inspection of cluster populations where cells begin in the main cluster body (ROIs 10,15) and traverse to the infected cluster (ROIs 1-4) where there is punctate viral signal (ROI 1) which progress to isolated infected cells characterized by homogenous NP staining throughout the cytoplasm (ROI 2), and ends with infection of surrounding cells and the formation of syncytia (ROIs 3,4). All efficacious compounds deplete ROIs 1-4 and thioguanine, clofazimine, S1RA and gilteritinib show differences in the UMAP cluster dynamics (Supplementary Figure 3) suggestive of different MOAs.

Lactoferrin blocks SARS-CoV-2 replication at different stages of the viral cycle

One of the most efficacious hits identified from our screen was lactoferrin, a protein found in milk and other secretory fluids[13]. We determined that lactoferrin has dose-dependent antiviral activity through a range of MOIs (Figure 4a and b). Previous work on lactoferrin in the context of infection with SARS-CoV-1 suggests that it blocks viral entry by binding heparan sulfate proteoglycans that are important for early viral attachment[14]. Our studies showed that lactoferrin blocks SARS-CoV-2 infection through entry inhibition and is also capable of rescuing infection when added 1 or 24 hrs p.i. (Figure 4b). Lactoferrin has been proposed to enhance innate interferon responses to limit viral replication within host cells[15]. Upon treatment, we observed a dose-dependent reduction of viral replication (Figure 4c), which was consistent with elevated mRNA levels of IFNβ and

interferon-stimulated genes (ISG15, MX1, Viperin and IFITM3) in lactoferrin-treated Huh7 cells (Figure 4d). Interestingly, we detected a robust antiviral effect by both holo and apolactoferrin (human and bovine), the latter being the component of widely available dietary supplements. To rule out a mode of action that involved a general iron depletion mechanism, we tested the protein transferrin and found that it was devoid of any anti-SARS-CoV-2 activity at the highest concentration of 2.3 µM (Figure 4e).

A clinically effective strategy for antiviral therapies uses a combinatorial (or "drug cocktail") approach, where compounds with varying MOAs are concomitantly used to target different stages in the viral life cycle and to minimize the risk of drug resistance from single-agent selective pressure. This is especially true for RNA viruses, which are highly variable and can develop drug-resistance[16]. Given the pronounced single-agent efficacy of lactoferrin, we tested whether combinations with remdesivir or hydroxycholoroquine could improve the overall antiviral activity. We found that lactoferrin potentiates the efficacy of both remdesivir (Figure 4f and Supplementary Figure 4a) and hydroxychloroquine (Figure 4f and Supplementary Figure 4f), which are currently explored treatments for SARS-CoV-2 infection. Therefore, combination therapy with lactoferrin could be beneficial in the management of the COVID-19 pandemic by reducing toxicity (e.g., hydroxycholorquine) or consumption (e.g., remdesivir).

Lead compounds demonstrate efficacy in iPSC-derived model of bronchial epithelium

To evaluate the translatability of our identified lead compounds, we used a biomimetic model of bronchial epithelium, iPSC-derived alveolar epithelial type 2 cells (iAEC2s)[17]. Surfactant protein C positive (SFTPC+) epithelial cells were previously used to model other lung diseases in place of primary AEC2s[18]. The advantage of using iPSC-derived AEC2s consists in the development of

an heterogeneous populations that contains also alveolar type II cells, the latter being involved in COVID-19 pathogenesis[19]. We demonstrated that iAECs are amenable to infection with an MOI of 10, resulting in about 50-60% infected cells. Acetylated tubulin staining revealed variable cytoskeleton structures, reminiscent of different cell types, and interesting protrusions that co-stained with viral marker NP. Morphology of infected cells also have key differences as compared to other cell types used in our study; particularly, the proportion of individually infected cells are greater than viral syncytia (Figure 5b). Remarkably, even at a high MOI of 10, dose-responsive antiviral activity was observed with bovine lactoferrin (IC_{50} = 45 nM), human lactoferrin (IC_{50} = 466 nM), S1RA (IC_{50} = 1 μM), and remdesivir (IC_{50} = 18 nM) (Figure 5a). This physiologic relevant model is a proxy of human lung tissue and serves as an intermediate model to further validate clinical potential of our identified lead compounds prior to *in vivo* studies.

DISCUSSION

In this study, we developed an experimental workflow based on high-content imaging and morphological profiling that allows for rapid screening of FDA-approved compounds, leveraging machine learning to determine potential MOA. We identified 17 FDA-approved compounds that limit SARS-CoV-2 infection *in vitro*. Of these, six were previously reported and serve as a benchmark validation of our endpoints and experimental approach, and eleven were hitherto unknown. We demonstrate that this approach is versatile (i.e., it can be applied to both transformed and more physiologically-relevant non-transformed cell lines) and can identify the emergent properties of the infection as well as novel phenotypes that can be perturbed through chemical inhibition.

A high-content morphological cell profiling approach is superior to image cytometry (tabulating percent positive) and plate reader assays for selecting and prioritizing drugs for repurposing. Here,

viral staining is not merely an absolute measure for viral infection (or inhibition) but the starting point for a detailed investigation of infection trajectories and observations of numerous phenotypic targets, including inhibition of syncytia formation, viral entry, or viral replication, and modulation of the host cell. We report compounds with strong antiviral activity against SARS-CoV-2 and also their putative MOA.

The UMAP embedding was highly effective for visualizing the infected cell population and the progression of the viral infection trajectory was clearly visible. We gained insight into the putative antiviral MOAs via inspection of the cluster populations. For thioguanine and clofazimine, increasing concentrations appear to suppress isolated single infected cells (ROI 4) while a small number of syncytia (ROI 3) are still observable (Supplementary Figure 3b), suggesting a replication inhibition MOA. This observation is consistent with the established MOA of both drugs as inhibitors of nucleic acid synthesis[20,21]. S1RA reduces ROIs 1-4 evenly, but ROI 13 increases (Supplementary Figure 3b: S1RA) and is characterized by increased cytoplasmic nucleic acid staining (Supplementary Figure 3a: ROI 13), suggesting a host-modulation MOA. Lastly, gilteritinib demonstrates an increase in ROI 12 with treatment (Supplementary Figure 3b: gilteritinib), a cell cluster defined by large and distributed lipid accumulation (Supplementary Figure 3a: ROI 12). Lipid accumulation, in liver-derived Huh7 cells, is associated with cytotoxicity and is consistent with reduction in viability with escalating dose (Figure 2b)[22].

Importantly, our study identified drugs that implicate new molecular targets/pathways in the pathogenesis of SARS-CoV-2 and produce clinically testable and readily translatable hypotheses. As an example, we observed dose-dependent antiviral activities of metoclopramide and domperidone, two potent dopamine receptor D2 antagonists used to treat gastroesophageal reflux disease and prevent other gastrointestinal symptoms, including nausea and vomiting[23]. Gastrointestinal symptoms have been increasingly reported in more than half of the patients

infected by SARS-CoV-2[2]. Notably, investigational drugs like hydroxychloroquine, lopinavir-ritonavir, tocilizumab and others can be associated with gastrointestinal and hepatic adverse events and hence are not ideal for patients already experiencing severe GI symptoms[24]. Metoclopramide and domperidone therefore represent a dual-target therapeutic option for COVID-19 patients. In contrast, the pro-dopaminergic drugs carbidopa, levodopa, and methyldopa promote infection (Supplementary Figure 2), suggesting that the dopamine pathway may contribute to infection outcomes. Additionally, all of the FDA-approved MEK inhibitors exacerbate viral infection 3-fold indicating a putative role of MEK in SARS-CoV-2 pathogenesis. These *in vitro* observations should be validated through clinical research that examines whether concomitant presence of drug and SARS-CoV-2 infection worsen COVID-19 symptoms.

As most FDA-approved drugs are optimized against human molecular targets, our screen helped identify crucial host factors involved in SARS-CoV-2 infection. Z-FA-FMK, an irreversible inhibitor of cysteine proteases, including cathepsins B, L, and S[25], exhibited potent antiviral activity. A recent report using a pseudovirus indicated cathepsin L is an entry factor of SARS-CoV-2[26]. The antiviral effect of Z-FA-FMK suggests that cathepsin L is a requirement also in the context of SARS-CoV-2 infection and suggests that this molecule could be a useful investigational tool to study virus entry. Similarly, fedratinib, approved by the FDA in 2019 for myeloproliferative neoplasm[27], is an orally bioavailable semi-selective JAK2 inhibitor. JAK-inhibitors have been proposed for COVID-19 to specifically inhibit TH17-mediated inflammatory responses. JAK-inhibitors have been proposed for COVID-19 treatment to specifically inhibit TH17-mediated inflammatory response[28,29] and to block numb-associated kinase responsible for clathrin-mediated viral endocytosis[30]. Several JAK-inhibitors are currently evaluated in clinical trials for COVID-19 management, including with baricitinib[31], jakotinib (ChiCTR2000030170), and ruxolitinib (ChiCTR2000029580). For their inhibitory effect on innate immune response at the

cellular level, JAK-inhibitors could serve as useful tools in the future to elucidate the involvement of the innate immune response in SARS-CoV-2 infection.

The sigma receptors (SigmaR1/R2) are permissive chaperones that mediate endoplasmic reticulum stress response and lipid homeostasis[32], processes that have been implicated in early stages of hepatitis C viral infection in Huh7 cells[33] and coronavirus pathogenesis[34]. We identified two sigma receptor modulators amiodarone[35], and S1RA[36] with potent antiviral activity, demonstrating IC_{50} values of 52 nM and 222 nM, respectively, with limited cell toxicity. Amiodarone is approved for treatment of arrhythmias but, like hydroxychloroquine, has potent cardiotoxic side effects through inhibition of the hERG ion channel[37] that limit therapeutic potential. S1RA has completed phase II clinical trials for the treatment of neuropathic pain[38,39]. Although Gordon *et al.* identified several other sigmaR1/R2 modulators that inhibited SARS-CoV-2 infection in Vero-E6 cells, antiviral activity for S1RA was not observed[40]. This suggests that the activity of S1RA is dependent on host cell factors specific to each cell line and, promisingly, that human cells may be more responsive to this compound, as observed in iAEC2s (Figure 5a).

Most noteworthy, our screen demonstrates lactoferrin as a SARS-CoV-2 inhibitor *in vitro* with multimodal efficacy. We showed dose-dependent efficacy in multiple cell types, including a non-transformed and clinically relevant iPSC-derived model of alveolar epithelium (Figure 4f). Lactoferrin gene expression has been shown previously to be highly upregulated in response to SARS-CoV-1 infection[41] and, in addition to enhancing natural killer cell and neutrophil activity, lactoferrin blocks viral entry through binding to heparan sulfate proteoglycans. Lactoferrin retains anti-SARS-CoV-2 activity 24 hrs p.i., which suggests additional MOA other than simple entry inhibition. Although we cannot conclude a definitive and complete MOA, we show significant host cell modulation through increased expression of several interferon-stimulated genes upon treatment with lactoferrin. Additionally, lactoferrin has been previously shown to decrease the

316 production of IL-6[42], which is one of the key players of the "cytokine storm" produced by SARS-
317 CoV-2 infection[43,44]. We found that lactoferrin, either from bovine or human origin, retain activity
318 in both the holo- and apo- forms, the latter being the component of orally available lactoferrin
319 supplements. Lactoferrin potential is heightened by its ability to mitigate a high MOI SARS-CoV-
320 2 infection in iAEC2 (Figure 5). Orally available lactoferrin could be especially effective in resolving
321 the gastrointestinal symptoms that are present in COVID-19 patients[45]. The mechanisms may be
322 similar to how lactoferrin reduces human norovirus infection through induction of innate immune
323 responses[46], especially as lactoferrin gene polymorphisms are associated with increased
324 susceptibility to infectious diarrhea[47]. If lactoferrin reduces viral load in the GI tract, it could reduce
325 fecal-oral transmission of COVID-19[48].
326
327 Combination therapies are likely to be required for effectively treating SARS-CoV-2 infection, and
328 this approach has already shown promise. For example, combination therapy with interferon beta-
329 1b, lopinavir–ritonavir, and ribavirin showed efficacy against SARS-CoV-2 in a prospective, open-
330 label, randomized, phase 2 trial[49]. We show that lactoferrin potentiates the antiviral activity of both
331 remdesivir and hydroxychloroquine and could be used as a combination therapy with these drugs,
332 which are currently being used or studied for the treatment of COVID-19. Due to its wide
333 availability, limited cost, and lack of adverse effects, lactoferrin could be a rapidly deployable
334 option for both prophylaxis and the management of COVID-19. Likewise, ipratropium bromide, a
335 widely-used quaternary ammonium salt bronchodilator, holds promise as another agent for
336 combination therapies with potential to reduce bronchial viral burden.
337
338 Although our findings are promising, further studies are needed to confirm their efficacy in other
339 representative *in vitro* cell lines and/or clinical studies. UMAP analysis provides limited insight to
340 MOA and serve as a basis for future pharmacological studies specific to our compounds in
341 treatment of SARS-CoV-2. These studies are currently ongoing.

High-content morphological cell profiling for drug repurposing screening enabled the identification of both novel antivirals efficacious against SARS-CoV-2 and compounds that possibly exacerbate SARS-CoV-2 infection. Furthermore, in contrast to other drug repurposing studies, the assay reported here allowed for the identification of potential MOA, including host cell responses. Confirmation in iAEC2s suggest high clinical translatability of these compounds. This approach to preclinical testing has promise for identifying other anti-SARS-CoV-2 drugs, rationally designing therapeutic combinations with multiple MOAs, and deployment of optimized combinations in a rapid and systemic fashion.

Supplementary Information is available for this paper.

Correspondence and requests for materials should be addressed to jzsexton@umich.edu

ACKNOWLEDGEMENTS

Funding: University of Michigan Institute for Clinical and Health Research (MICHR) (NCATS - UL1TR002240) and its Center for Drug Repurposing. JZS is supported by the National Institute of Diabetes and Digestive and Kidney Diseases (R01DK120623). JWW is supported by the pharmacological sciences training program (PSTP) T32 training grant. CM is supported by Marie-Slodowska Curie individual fellowship (GA - 841247) and MICHR Postdoctoral Translational Scholars Program. KDA is supported by the I.M. Rosenzweig Junior Investigator Award from the Pulmonary Fibrosis Foundation. JRS is supported by the National Heart, Lung, and Blood Institute (NHLBI – R01HL119215), by the NIAID Novel Alternative Model Systems for Enteric Diseases (NAMSED) consortium (U19AI116482) and by grant number CZF2019-002440 from the Chan Zuckerberg Initiative DAF, an advised fund of Silicon Valley Community Foundation.

The authors would like to thank Matthew Chess for Amazon AWS support, Kevin Jan and Peyton Uhl at Yokogawa for imaging support, Nick Santoro at the University of Michigan Center for Chemical Genomics. We thank David Egan and Wienand Omta from Core Life Analytics for assisting high content data analytics as well as Philip Cheung and Brian Bolt at ReFactor Biosciences for assistance with HTS data registration. Finally, we thank Tracey Schultz and Dianne Jazdzyk for project management.

METHODS

Cells and virus. Vero E6, Caco-2 and Huh7 cells were maintained at 37°C with 5% CO2 in Dulbecco's Modified Eagle's Medium (DMEM; Welgene), supplemented with 10% heat-inactivated fetal bovine serum (FBS), HEPES, non-essential amino-acids, L-glutamine and 1X

Antibiotic-Antimycotic solution (Gibco). iPSC (SPC2 iPSC line, clone SPC2-ST-B2, Boston University) derived alveolar epithelial type 2 cells (iAEC2s) were differentiated as previously described and maintained as alveolospheres embedded in 3D Matrigel in "CK+DCI" media, as previously described (Jacob et al. 2019). iAEC2s were passaged approximately every two weeks by dissociation into single cells via the sequential application of dispase (2mg/ml, Thermo Fisher Scientific, 17105-04) and 0.05% trypsin (Invitrogen, 25300054) and re-plated at a density of 400 cells/µl of Matrigel (Corning, 356231), as previously described (Jacob et al. 2019). SARS-CoV-2 WA1 strain was obtained by BEI resources and was propagated in Vero E6 cells. Viral titers were determined by TCID50 assays in Vero E6 cells (Reed and Muench method) by microscopic scoring. All experiments using SARS-CoV-2 were performed at the University of Michigan under Biosafety Level 3 (BSL3) protocols in compliance with containment procedures in laboratories approved for use by the University of Michigan Institutional Biosafety Committee (IBC) and Environment, Health and Safety (EHS).

Viral titer determination. Vero E6, Caco-2 and Huh7 cells were seeded in a 48-well plate at 2x10^4 cells/well incubated overnight at 37°C with 5% CO2. Cells were then infected with SARS-CoV-2 WA1 at a multiplicity of infection (MOI) of 0.2. One hour after infection, cells were harvested (day 0 of infection) or kept at 37°C for 1, 2 and 3 days p.i. Viral titer determination was performed by TCID50 assay on Vero E6 cells of the total virus (supernatant and intracellular fraction). Alternatively, cells were harvested with Trizol and total cellular and viral RNA was extracted with the ZymoGen Direct-zol RNA extraction kit. Viral RNA was quantified by RT-qPCR using the 2019-nCoV CDC qPCR Probe Assay and the probe set N1 (IDT technologies). IFNβ, viperin, MX1, ISG15, IFITM3 and the housekeeping gene GAPDH mRNA levels were quantified by qPCR with SsoAdvanced™ Universal SYBR® Green Supermix (Bio-Rad) with specific primers (IFNβ: F-TTGACATCCCTGAGGAGATTAAGC, R- TCCCACGTACTCCAACTTCCA; MX1: F-CCAGCTGCTGCATCCCACCC, R-AGGGGCGCACCTT CTCCTCA; ISG15: F-

TGGCGGGCAACGAATT, R- GGGTGATCTGCGCCTTCA; IFITM3: F-TCCCAC GTACTCCAACTTCCA, R-AGCACCAGAAACACGTGCACT; GAPDH: F-CTCTGCTCCTCCTGTTCGAC, R-GCGCCCCACCAAGCTCAAGA). Fold increase was calculated by using the ΔΔCt method over non-infected untreated Huh7.

Viral infectivity assay. 384-well plates (Perkin Elmer, 6057300) were seeded with Huh7 cells at 3000 cells/well and allowed to adhere overnight. Compounds were then added to the cells and incubated for 4 hours. The plates were then transferred to BSL3 containment and infected with SARS-CoV-2 WA1 at a multiplicity of infection (MOI) of 0.2 in a 10 µL addition with shaking to distribute virus. For the final dose-responses curves, porcine trypsin (Sigma-Aldrich, T0303) at a final concentration of 2µg/ml was included during infection. After one hour of absorption, the virus inoculum was removed, and media replaced with fresh compound. Uninfected cells and vehicle-treated cells were included as positive and negative control, respectively. Two days post-infection, cells were fixed with 4% PFA for 30 minutes at room temperature, permeabilized with 0.3% Triton X-100 and blocked with antibody buffer (1.5% BSA, 1% goat serum and 0.0025% Tween 20). The plates were then sealed, surface decontaminated, and transferred to BSL2 for staining with the optimized fluorescent dye-set: anti-nucleocapsid protein (anti-NP) SARS-CoV-2 antibody (Antibodies Online, Cat# ABIN6952432) overnight treatment at 4C followed by staining with secondary antibody Alexa-647 (goat anti-mouse, Thermo Fisher, A21235), Hoechst-33342 pentahydrate (bis-benzimide) for nuclei staining (Thermo FIsher, H1398), HCS LipidTOX™ Green Neutral Lipid Stain (Thermo Fisher, H34475), and HCS CellMask™ Orange for cell delineation (Thermo Fisher H32713). iAEC2 maintained in 3D culture were dissociated to single cells and seeded in collagen coated 384-well plates at a seeding density of 8000 cells/well in the presence of 10 µM Y-27632 for the first 72 hours after plating (APExBIO, A3008 to grow to roughly 80% confluence. Infection was performed at MOI of 10 in the presence of 2µg/ml of trypsin porcine

(Sigma-Aldrich, T0303). Staining protocol for the iAEC2s differed slightly with the addition of an anti-acetylated tubulin primary antibody (Cell Signaling, 5335), instead of HCS CellMask Orange, and the use of an additional secondary Alexa 488 antibody (donkey anti-rabbit, Jackson ImmunoResearch, 711-545-152).

Multi-cycle cytopathogenic effect (CPE) reduction assay. Vero E6 were allowed to adhere overnight in 96-well cell culture plates. A 1:2 10-point serial dilution of compounds (5000nM-5nM) and SARS-CoV-2 at MOI of 0.002 were added. CPE was evaluated by microscopic scoring at 5dpi. The 50% inhibitory concentration (IC50) was calculated by logarithmic interpolation and is defined as the concentration at which the virus-induced CPE is reduced by 50%.

Compound library. The compound library deployed for drug screening was created using the FDA-Approved Drugs Screening Library (Item No. 23538) from Cayman Chemical Company. This library of 875 compounds was supplemented with additional FDA approved drugs and rationally included clinical candidates from other vendors including MedChemExpress, Sigma Aldrich, and Tocris. Our library was formatted in five 384-well compound plates and was dissolved in DMSO at 10 mM. Hololactoferrin (Sigma Aldrich, L4765), apolactoferrin (Jarrow Formulas, 121011), native human lactoferrin (Creative BioMart, LFT-8196H) and transferrin (Sigma Aldrich, T2036) were handled separately and added manually in cell culture media. Dilution plates were generated for qHTS at concentrations of 2 mM, 1 mM, 500 μM, 250 μM and 50 μM and compounds were dispensed at 1:1000 dilution.

qHTS primary screen and1sonse confirmation. For the qHTS screen, compounds were added to cells using a 50 nL pin tool Caliper Life Sciences Sciclone ALH 3000 Advanced Liquid Handling system at the University of Michigan Center for Chemical Genomics (CCG). Concentrations of 2

μM, 1 μM, 500 nM, 250 nM and 50 nM were included for the primary screen. Post qHTS screen, all compounds were dispensed using an HP D300e Digital Compound Dispenser and normalized to a final DMSO concentration of 0.1% DMSO. Confirmation dose response was performed in triplicate and in 10-point:2-fold dilution.

Imaging. Stained cell plates were imaged on both Yokogawa CQ1 and Thermo Fisher CX5 high content microscopes with a 20X/0.45NA LUCPlan FLN objective. Yokogawa CQ1 imaging was performed with four excitation laser lines (405nm/488nm/561nm/640nm) with spinning disc confocal and 100ms exposure times. Laser power was adjusted to yield optimal signal to noise ratio for each channel. Maximum intensity projection images were collected from 5 confocal planes with a 3 micron step size. Laser autofocus was performed and nine fields per well were imaged covering approximately 80% of the well area. The Thermofisher CX5 with LED excitation (386/23nm, 485/20nm, 560/25nm, 650/13nm) was also used and exposure times were optimized to maximize signal/background. Nine fields were collected at a single Z-plane as determined by image-based autofocus on the Hoechst channel. The primary qHTS screen was performed using CX5 images and all dose-response plates were imaged using the CQ1.

Image segmentation and feature extraction. The open source CellProfiler software was used in an Ubuntu Linux-based distributed Amazon AWS cloud implementation for segmentation, feature extraction and results were written to an Amazon RDS relational database using MySQL. A pipeline was developed to automatically identify the nuclei, cell, cytoplasm, nucleoli, neutral lipid droplets and syncytia for feature extraction. Multiple intensity features and radial distributions were measured for each object in each channel and cell size and shape features were measured. Nuclei were segmented using the Hoechst-33342 image and the whole cell mask was generated by expanding the nuclear mask to the edge of the Cell Mask Orange image.

Data pre-processing. Cell level data were pre-processed and analyzed in the open source Knime analytics platform[50]. Cell-level data was imported into Knime from MySQL, drug treatment metadata was joined, and features were centered and scaled. Features were pruned for low variance (<5%) and high correlation (>95%) and resulted in 660 features per cell.

Statistical methods and hypothesis testing. Dose-response curves were fit and pairwise differences between experimental conditions were tested using Prism (Graphpad Software, San Diego, CA, USA). Other statistical tests were performed in the statistical programming language and environment R.

Machine learning - infectivity score and field-level scoring. Multiple logistic regression as implemented in the statistical language and environment R was used to identify features characteristic of cells within infected wells. Models were fit to cells from infected and uninfected control wells in the first five plate-series of the quantitative high throughput screen. As an independent benchmark, these logistic regression models were validated against a manually selected set of individual infected and uninfected cells; features which degraded performance on the benchmark were excluded from the model. The final model included only virus channel intensity features in the cell and cytoplasm ROIs. As a threshold for initial classification, the minimum value from virus-infected cells in the benchmark was used; the final decision rule is given in Eq. 1.

(Eq.1) : A cell is infected if (Cells_Intensity_IntegratedIntensityEdge_Virus × 0.1487025 +
Cells_Intensity_MeanIntensityEdge_Virus × -38.40196 +
Cells_Intensity_MaxIntensityEdge_Virus × 42.70269 +
Cytoplasm_Intensity_StdIntensity_Virus × 42.54849) ≥ 1.525285

Then, individual field images from the infected control were categorized as confirmed-infected when the mean feature values, across all cells in the field, were above the threshold in Eq. 1. Using mean values for all 660 cell-profiler features in each field, a random forest classifier was trained to predict a probability of membership in the category of uninfected control fields vs confirmed-infected fields. The output of this random forest classifier is reported as "Probpos" (for the positive, uninfected control), throughout. Field level mean/median feature values were computed and a random forest model was fit between the positive control (32 uninfected wells) and the negative control (32 infected wells, 0.1% DMSO vehicle treated) with 80/20 cross validation. The compound treated wells were scored with the RF model and the efficacy score was normalized to the individual plate.

UMAP embedding. The embed_umap application of MPLearn (v0.1.0, https://github.com/momeara/MPLearn) was used to generate UMAP embeddings. Briefly, each for a set of cells, each feature was per-plate standardized and jointly orthogonalized using sklearn.IncrementalPCA(n_components=379, batch_size=1000). Then features were embedded into 2-dimensions using umap-learn (v0.4.1)[12] with umap. UMAP(n_components=2, n_neighbors=15, min_dist=0, init='spectral', low_memory=True). Embeddings were visualized using Holovies Datashader (v1.12.7)[51], using histogram equalization and the viridis color map. Visualizing subsets was done in JMP Pro 14.

Data analytics. HC Stratominer (Core Life Analytics, Utrecht NL) was used as an independent method for hit-calling and performs fully automated/streamlined cell-level data pre-processing and score generation. IC Stratominer was also used to fit dose response curves for qHTS. Compound registration and assay data registration were performed using the open source ACAS platform (Refactor BioSciences github https://github.com/RefactorBio/acas).

Dose-response analysis and compound selection. In qHTS screening, a compound was selected to be carried forward into full dose response confirmation when meeting one of the following criteria: 1) Probpos greater than 0.75 for the median field in at least three concentrations, with per-field cell counts at least 60% of the positive control, and without an observed standard deviation in Probpos across-fields-in-the-well of 0.4 or greater, 2) a dose-response relationship with Probpos was observed (by inspection) across the five concentrations tested, including compounds with Propbos greater than 0.90 at the two highest concentrations, or 3) compounds of interest not meeting this criteria were carried forward if reported positive in the literature or were being evaluated in clinical trials for COVID-19.

Dose response analysis in the confirmation and combinatorial screening. Due to the spatial inhomogeneity of infected cells across a single well, approximately half of the fields were undersaturated, leading to a consistent distribution in Probpos that saturates in the top third of 27 rank-ordered fields (from 9 fields and triplicate wells) for each concentration tested. The Probpos effect for a compound concentration was tabulated by averaging the top third of rank ordered fields. Outlier fields with high Probpos values were visually inspected and eliminated if artifacts (segmentation errors or debris) were observed. Cells treated with known fluorescence drugs

including Clofazimine, were confirmed to not have spectral interference. Dose response curves were fit with Graphpad Prism using a semilog 4-parameter variable slope model.

FIGURES AND LEGENDS

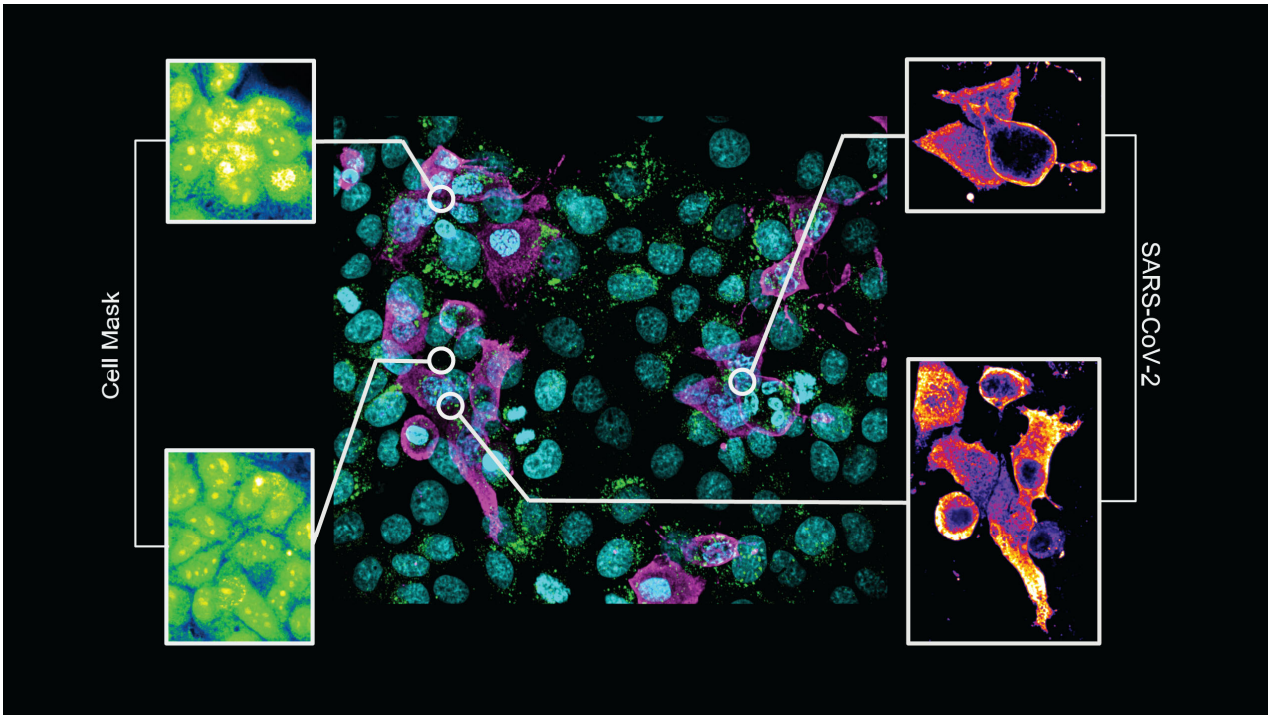

Figure 1. Morphological profiling of SARS-CoV-2 infected Huh7 cells (MOI of 0.2 for 48 hrs). Center image: representative field with nuclei (cyan), neutral lipids (green), and SARS-CoV-2 NP (magenta). Through feature extraction key traits of SARS-CoV-2 infection were characterized with multinucleated syncytia (top left) and abundant nucleoli (bottom left) from HCS CellMask Orange channel. Cell viral compartmentalization (top right) with cytoplasmic protrusions (bottom right) from SARS-CoV-2 NP channel. Representative image was acquired on a Yokogawa CQ1 high-content imager and visualized with Fiji ImageJ package.

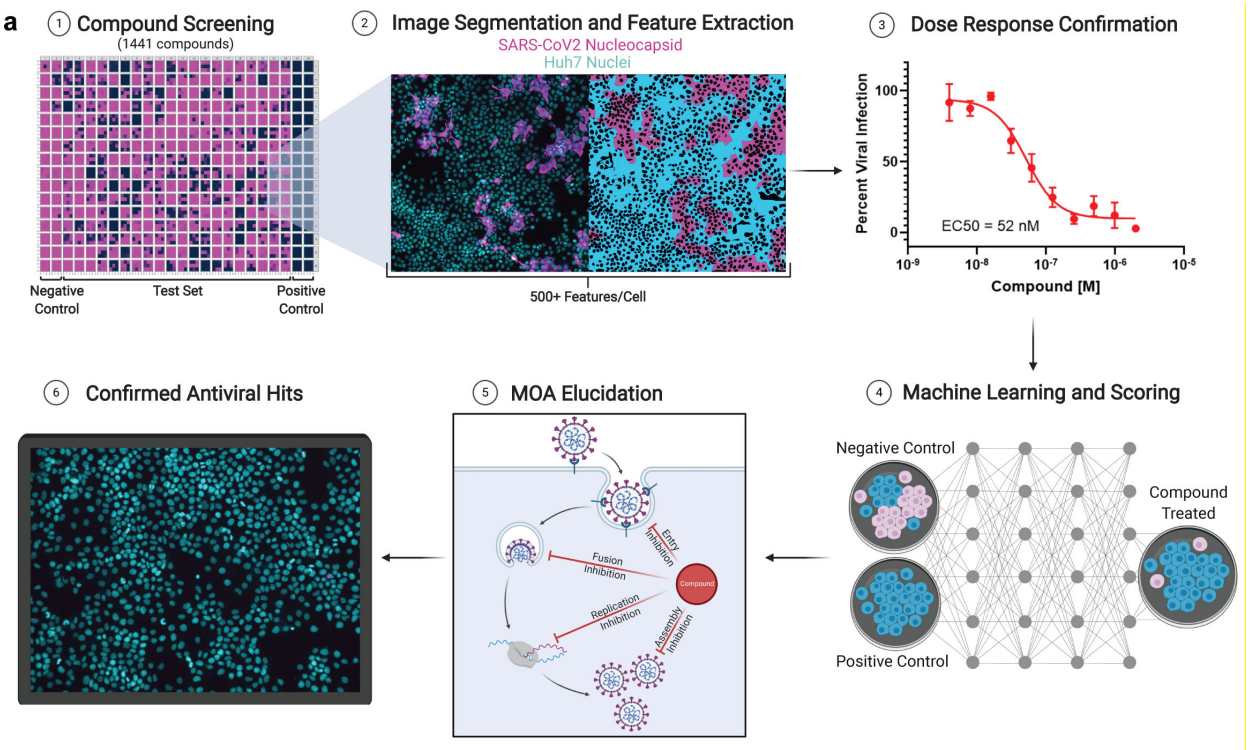

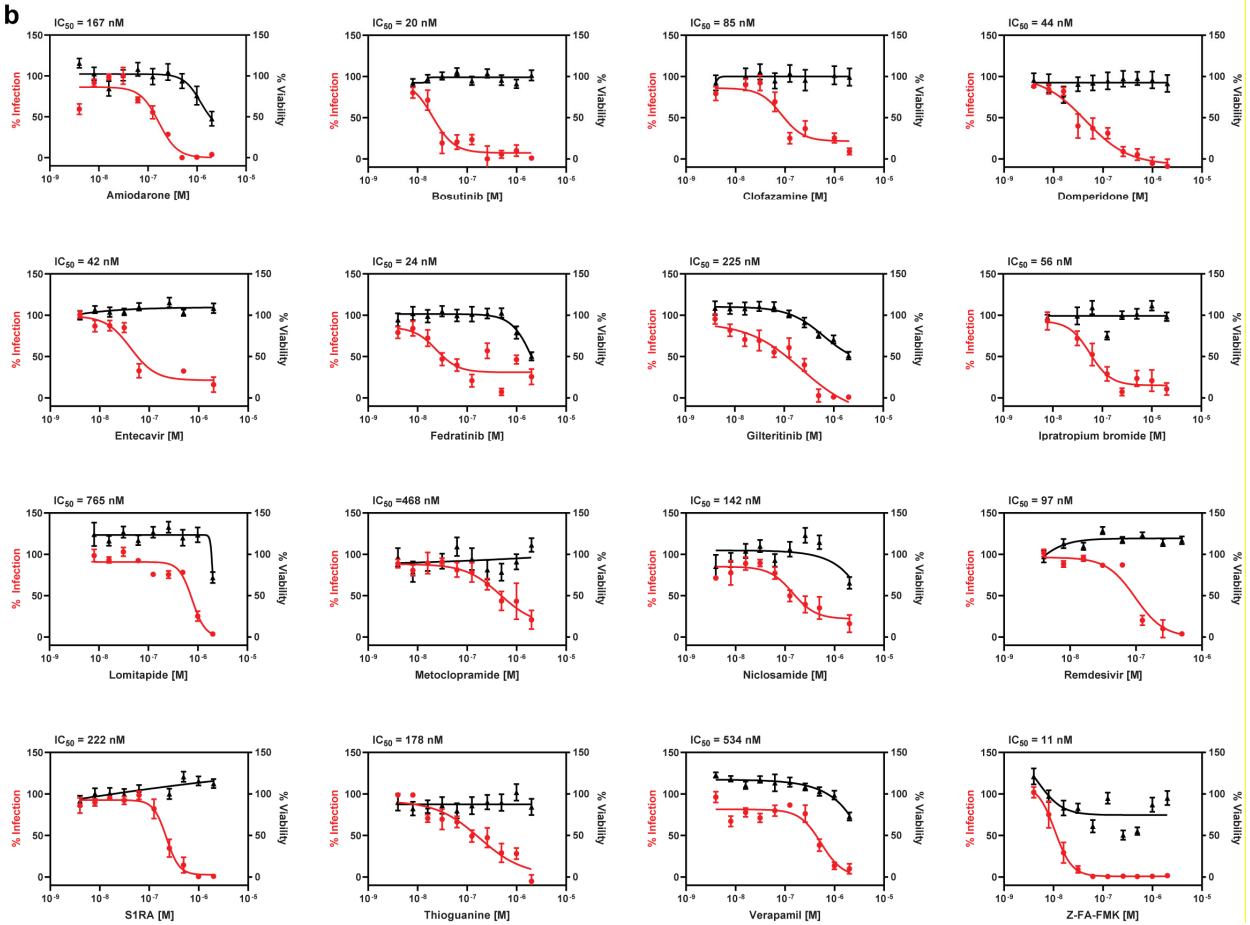

589 **Figure 2**. a) Schematic representation of the anti-SARS-CoV-2 therapy discovery effort. 1)
590 Compounds are administered to cells cultured on 384-well plates infected with SARS-CoV-2.
591 Each plate contains 24 negative (infected) and 24 positive (non-infected) control wells to adjust
592 for plate-to-plate variation. 2) Cells are fixed, stained, and imaged. Images are analyzed through
593 a Cell Profiler-based pipeline which segments nuclei, cell boundaries, neutral lipid content and
594 viral syncytia formation while extracting features of these cellular compartments. 3) Dose-
595 response curves are calculated through multivariate-analysis to define per-image viral infectivity
596 4) Machine learning models are built around positive and negative control wells based on
597 extracted features and applied to each drug condition. 5) Models inform on individual compound
598 mode(s) of antiviral action through obtained features 6) confirmed antiviral hits; b) Dose-response
599 curves of 16 hits of the drug screening. Graphs represent median SEM of 10-point 1:2 dilution
600 series of selected compounds for N=3 biological replicates. IC_{50} were calculated based on
601 normalization to the control and after fitting in GraphPad Prism.
602

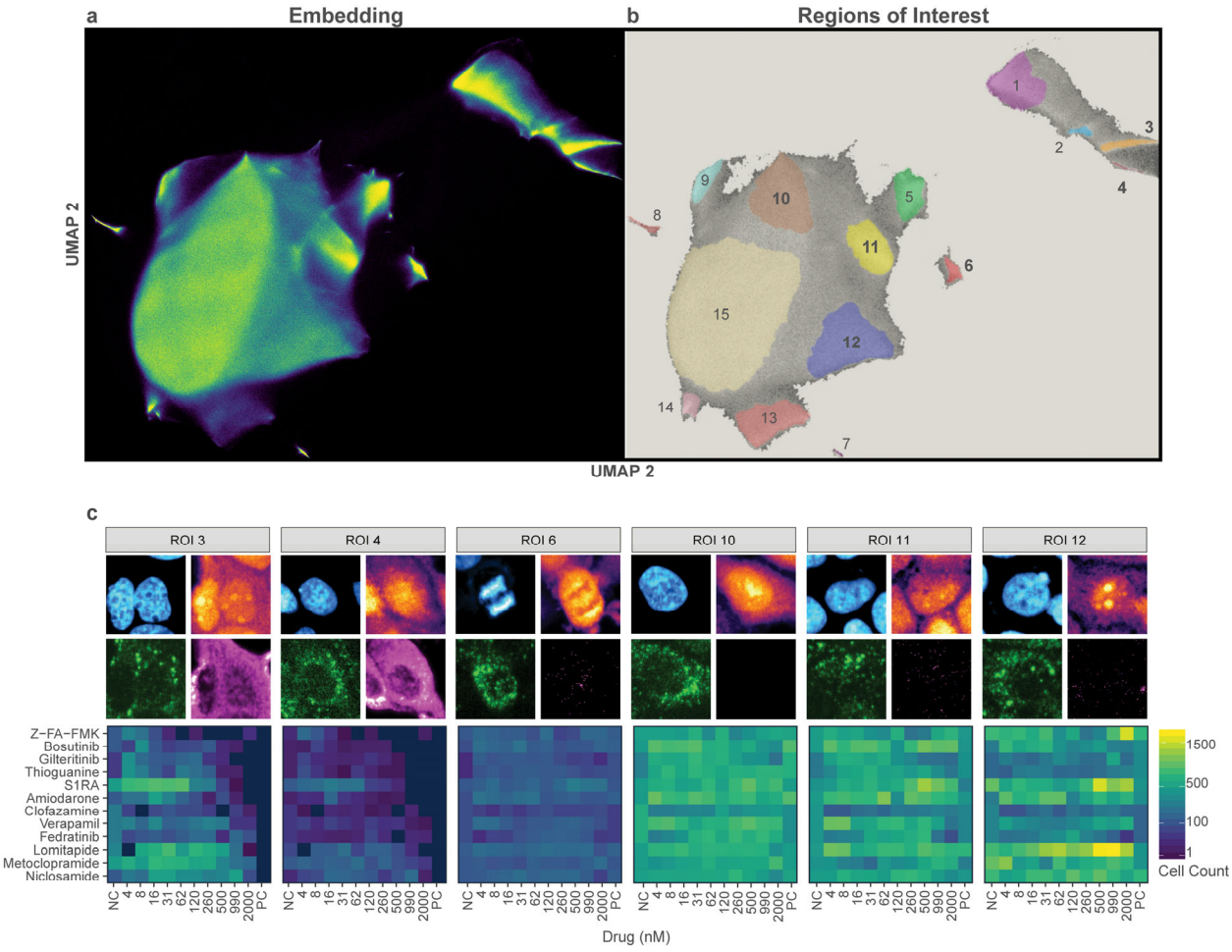

Figure 3. a) 2 dimensional UMAP embedding of two million individual cells by 379 morphological features consisting of uninfected (PC), infected (NC), or infected and treated with 12 FDA approved and clinical candidate drug screening hits across 10 doses. b) Cluster regions of interest (ROI) in the UMAP are highlighted including infected syncytial (ROI 3) and isolated (ROI 4) cells and non-infected mitotic (ROI 6), normal (ROI 10), scattered lipid (ROI 11), and cytoplasm punctate (ROI 12) cells. c) For six ROIs, a representative cell is shown by nuclear (upper-left), cell boundary (upper-right), neutral lipid (lower-left), and SARS-CoV-2 NP (lower-right) channels. Below, the cell count across each treatment and dose is shown as a heat-map, where the dose-responsive behavior for ROIs 3 and 4 are visible.

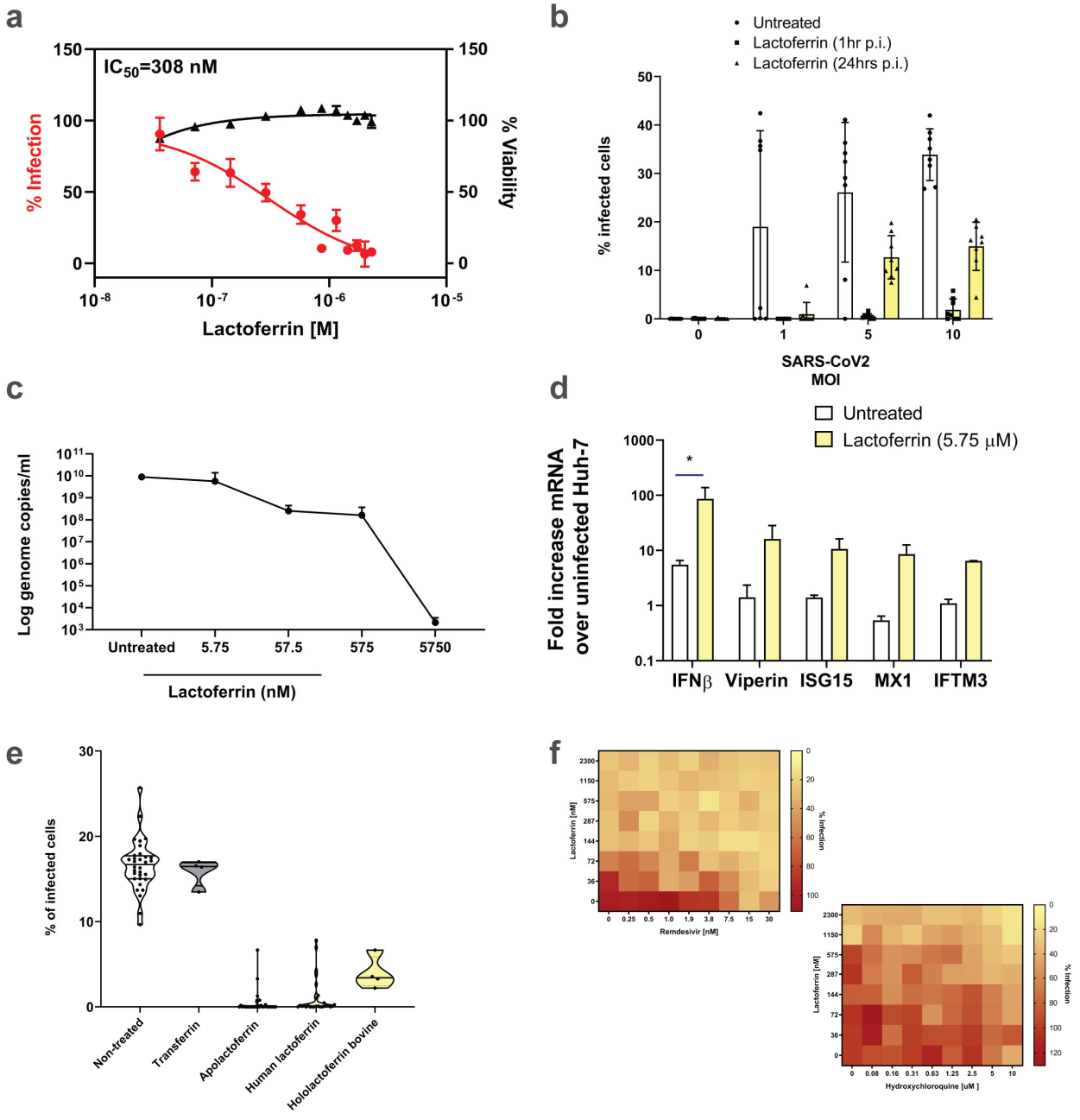

Figure 4. Lactoferrin blocks SARS-CoV-2 replication at different stages of the viral cycle. a) Huh7 cells were treated with lactoferrin (0 to 2.3 μM) and infected with SARS-CoV-2 (MOI of 0.2) in a 384-well plate. Plates were imaged using automated fluorescence microscopy and processed using our image analysis pipeline to determine percent viral inhibition. Graph indicates a dose-response (RED, IC_{50} = 308 μM). Cell viability is depicted in black. b) Huh7 were infected with SARS-CoV-2 (MOI of 1, 5 and 10; MOI of 0 indicates non-infected cells) and treated with 2.3 μM

of lactoferrin at 1 and 24 hrs p.i. Bars indicate the percentage of infected cells in different conditions. Data is an average of eight replicates. Statistical significance determined using multiple student's t-test with the Bonferroni-Dunn method, with alpha = 0.05. Except for MOI of 0, all conditions (Untreated *vs* Lactoferrin, 1 hr or Untreated *vs* Lactoferrin, 24 hr) differ at $P<0.0001$. c-d) $2.5x10^4$ Huh7 cells were infected with SARS-CoV-2 at MOI of 0.2. 48 hrs p.i., cells were harvested and RNA was extracted. Viral genome copies were calculated with an absolute quantification method (standard curve) (c) and mRNA levels of cellular IFNβ, MX1, ISG15 and IFITM3 (d) were calculated with ΔΔCt over non-infected Huh7. Data are average, SD of N=2 biological replicates with n=3 technical replicates each. Statistical significance determined using multiple student's t-test with the Bonferroni-Dunn method, with alpha = 0.05. *$P<0.001$. e) Percentage of SARS-CoV-2 infected Huh7 cells upon treatment with bovine apolactoferrin and hololactoferrin, native human lactoferrin and transferrin at a concentration of 2.3 μM. f) 2-dimensional dose response heat maps of lactoferrin (0 to 2.3 μM) in combination with remdesivir and hydroxychloroquine (0 to 30 nM and 0 to 10 μM, respectively). Remdesivir combination was evaluated with a 0.2 MOI and HCQ was evaluated with a MOI of 10 leading to a relative shift in lactoferrin potency.

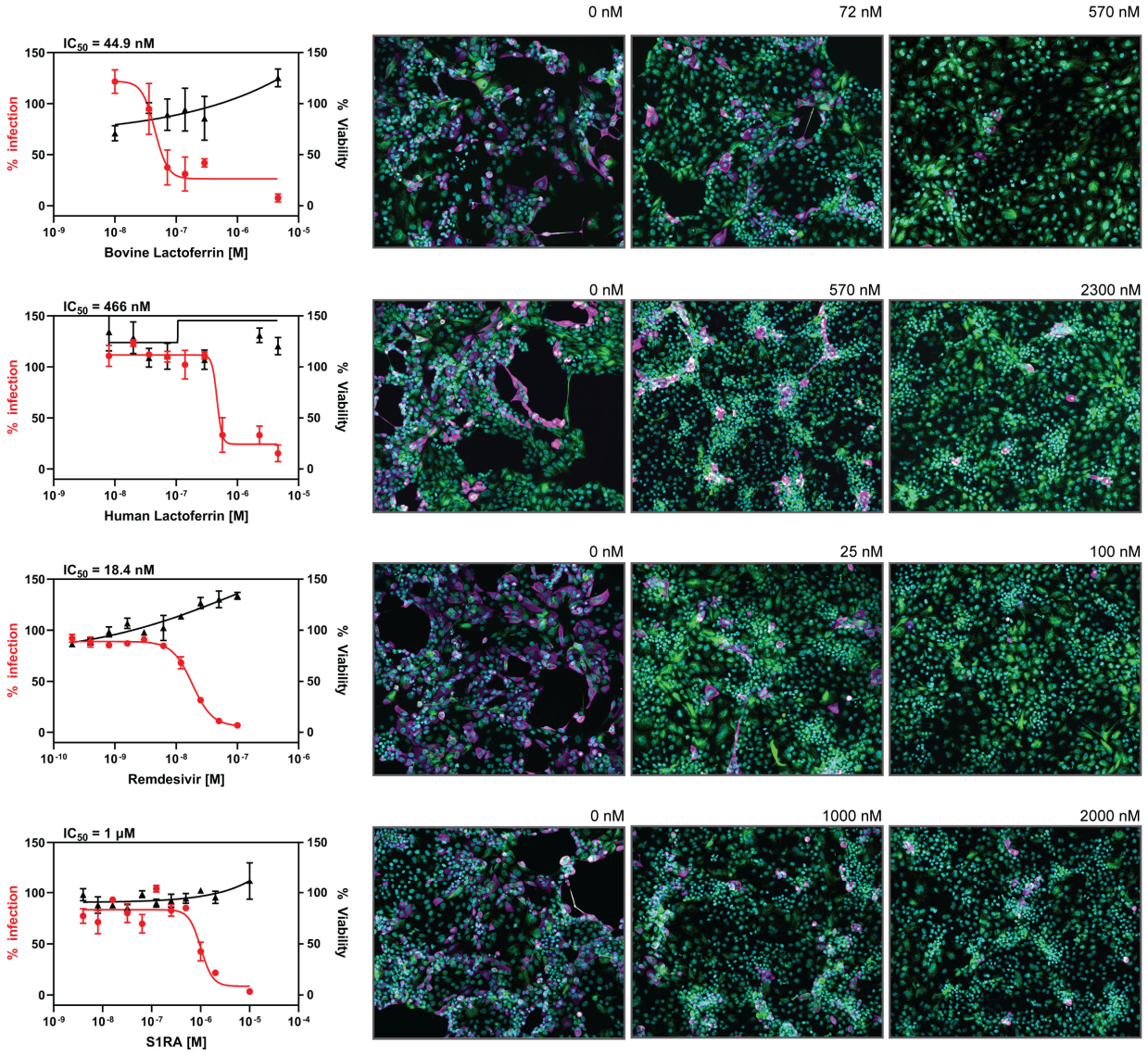

Figure 5. Antiviral activity of selected compounds was assessed in iAEC2 cells infected with SARS-CoV-2 at MOI 10. Bovine and human lactoferrin exhibited IC_{50} of 44.9 and 466 nM respectively. Remdesivir and S1RA exhibited IC_{50} of 18.4 nM and 1 µM respectively. Images of nuclei (cyan), acetylated tubulin (green), and NP (magenta) from non-treated infected control, IC_{50}, and IC_{max}.

SUPPLEMENTARY INFORMATION

Supplementary Figure 1: Screening assay optimization

Supplementary Figure 2: Compounds exacerbating SARS-CoV2 infection

Supplementary Figure 3: Features of UMAP regions of interest (ROI)

Supplementary Figure 4: Combinatory effects of remdesivir and hydroxycholoroquine with lactoferrin

Supplementary Table 1: Compound Deep Dives

Supplementary File 1: Compound library details

Supplementary File 2: 3D reconstruction video of infected cells

REFERENCES

1. Xiao, F. *et al.* Evidence for Gastrointestinal Infection of SARS-CoV-2. *Gastroenterology* (2020). doi:10.1053/j.gastro.2020.02.055

2. Lin, L. *et al.* Gastrointestinal symptoms of 95 cases with SARS-CoV-2 infection. *Gut* (2020). doi:10.1136/gutjnl-2020-321013

3. Avula, A. *et al.* COVID-19 presenting as stroke. *Brain. Behav. Immun.* (2020). doi:10.1016/j.bbi.2020.04.077

4. Kochi, A. N., Tagliari, A. P., Forleo, G. B., Fassini, G. M. & Tondo, C. Cardiac and arrhythmic complications in patients with COVID-19. *Journal of Cardiovascular Electrophysiology* (2020). doi:10.1111/jce.14479

5. Mulangu, S. *et al.* A randomized, controlled trial of Ebola virus disease therapeutics. *N. Engl. J. Med.* (2019). doi:10.1056/NEJMoa1910993

6. Oprea, T. I. *et al.* Drug repurposing from an academic perspective. *Drug Discovery Today: Therapeutic Strategies* (2011). doi:10.1016/j.ddstr.2011.10.002

7. Chu, H. *et al.* Comparative tropism, replication kinetics, and cell damage profiling of SARS-CoV-2 and SARS-CoV with implications for clinical manifestations, transmissibility,

and laboratory studies of COVID-19: an observational study. *The Lancet Microbe* (2020). doi:10.1016/s2666-5247(20)30004-5

8. Hoffmann, M. *et al.* SARS-CoV-2 Cell Entry Depends on ACE2 and TMPRSS2 and Is Blocked by a Clinically Proven Protease Inhibitor. *Cell* (2020). doi:10.1016/j.cell.2020.02.052

9. Riva, L. *et al.* A Large-scale Drug Repositioning Survey for SARS-CoV-2 Antivirals. *bioRxiv* (2020). doi:10.1101/2020.04.16.044016

10. Katie Heiser *et al.* Identification of potential treatments for COVID-19 through artificial intelligence enabled phenomic analysis of human cells infected with SARS-CoV-2. *bioRxiv* (2020). doi:10.1101/2020.04.21.054387

11. Jeon, S. *et al.* Identification of antiviral drug candidates against SARS-CoV-2 from FDA-approved drugs. *Antimicrob. Agents Chemother.* (2020). doi:10.1128/AAC.00819-20

12. McInnes, L., Healy, J., Saul, N. & Großberger, L. UMAP: Uniform Manifold Approximation and Projection. *J. Open Source Softw.* (2018). doi:10.21105/joss.00861

13. Lang, J. *et al.* Inhibition of SARS pseudovirus cell entry by lactoferrin binding to heparan sulfate proteoglycans. *PLoS One* (2011). doi:10.1371/journal.pone.0023710

14. Kell, D. B., Heyden, E. L. & Pretorius, E. The Biology of Lactoferrin, an Iron-Binding Protein That Can Help Defend Against Viruses and Bacteria . *Frontiers in Immunology* **11**, 1221 (2020).

15. Siqueiros-Cendón, T. *et al.* Immunomodulatory effects of lactoferrin. *Acta Pharmacologica Sinica* (2014). doi:10.1038/aps.2013.200

16. Yeni, P. Update on HAART in HIV. in *Journal of Hepatology* (2006). doi:10.1016/j.jhep.2005.11.021

17. Hurley, K. *et al.* Reconstructed Single-Cell Fate Trajectories Define Lineage Plasticity Windows during Differentiation of Human PSC-Derived Distal Lung Progenitors. *Cell Stem Cell* (2020). doi:10.1016/j.stem.2019.12.009

18. Jacob, A. *et al.* Derivation of self-renewing lung alveolar epithelial type II cells from human pluripotent stem cells. *Nat. Protoc.* (2019). doi:10.1038/s41596-019-0220-0

19. Mason, R. J. Pathogenesis of COVID-19 from a cell biology perspective. *European Respiratory Journal* (2020). doi:10.1183/13993003.00607-2020

20. Evans, W. E. Pharmacogenetics of Thiopurine S-Methyltransferase and Thiopurine Therapy. in *Therapeutic Drug Monitoring* (2004). doi:10.1097/00007691-200404000-00018

21. Arbiser, J. L. & Moschella, S. L. Clofazimine: A review of its medical uses and mechanisms of action. *Journal of the American Academy of Dermatology* (1995). doi:10.1016/0190-9622(95)90134-5

22. Alghamdi, S., Leoncikas, V., Plant, K. E. & Plant, N. J. Synergistic interaction between lipid-loading and doxorubicin exposure in Huh7 hepatoma cells results in enhanced cytotoxicity and cellular oxidative stress: Implications for acute and chronic care of obese cancer patients. *Toxicol. Res. (Camb).* (2015). doi:10.1039/c5tx00173k

23. Hibbs, A. M. & Lorch, S. A. Metoclopramide for the treatment of gastroesophageal reflux disease in infants: A systematic review. *Pediatrics* (2006). doi:10.1542/peds.2005-2664

24. Hajifathalian, K. *et al.* SARS-COV-2 infection (coronavirus disease 2019) for the gastrointestinal consultant. *World J. Gastroenterol.* (2020). doi:10.3748/wjg.v26.i14.1546

25. Roscow, O., Ganassin, R., Garver, K. & Polinski, M. Z-FA-FMK demonstrates differential inhibition of aquatic orthoreovirus (PRV), aquareovirus (CSRV), and rhabdovirus (IHNV) replication. *Virus Res.* (2018). doi:10.1016/j.virusres.2017.11.024

26. Ou, X. *et al.* Characterization of spike glycoprotein of SARS-CoV-2 on virus entry and its immune cross-reactivity with SARS-CoV. *Nat. Commun.* (2020). doi:10.1038/s41467-020-15562-9

27. Pardanani, A. *et al.* TG101209, a small molecule JAK2-selective kinase inhibitor potently inhibits myeloproliferative disorder-associated JAK2V617F and MPLW515L/K mutations.

Leukemia (2007). doi:10.1038/sj.leu.2404750

28. Wu, D. & Yang, X. O. TH17 responses in cytokine storm of COVID-19: An emerging target of JAK2 inhibitor Fedratinib. *J. Microbiol. Immunol. Infect.* (2020). doi:10.1016/j.jmii.2020.03.005

29. Zhang, W. *et al.* The use of anti-inflammatory drugs in the treatment of people with severe coronavirus disease 2019 (COVID-19): The experience of clinical immunologists from China. *Clinical Immunology* (2020). doi:10.1016/j.clim.2020.108393

30. Stebbing, J. *et al.* COVID-19: combining antiviral and anti-inflammatory treatments. *The Lancet Infectious Diseases* (2020). doi:10.1016/S1473-3099(20)30132-8

31. Treatment of Moderate to Severe Coronavirus Disease (COVID-19) in Hospitalized Patients. (2020). Available at: https://clinicaltrials.gov/ct2/show/NCT04321993.

32. Delprat, B., Crouzier, L., Su, T. P. & Maurice, T. At the Crossing of ER Stress and MAMs: A Key Role of Sigma-1 Receptor? in *Advances in Experimental Medicine and Biology* (2020). doi:10.1007/978-3-030-12457-1_28

33. Friesland, M., Mingorance, L., Chung, J., Chisari, F. V. & Gastaminza, P. Sigma-1 Receptor Regulates Early Steps of Viral RNA Replication at the Onset of Hepatitis C Virus Infection. *J. Virol.* (2013). doi:10.1128/jvi.03557-12

34. Fung, T. S. & Liu, D. X. Coronavirus infection, ER stress, apoptosis and innate immunity. *Frontiers in Microbiology* (2014). doi:10.3389/fmicb.2014.00296

35. Moebius, F. F., Reiter, R. J., Hanner, M. & Glossmann, H. High affinity of sigma1-binding sites for sterol isomerization inhibitors: Evidence for a pharmacological relationship with the yeast sterol C8-C7 isomerase. *Br. J. Pharmacol.* (1997). doi:10.1038/sj.bjp.0701079

36. Díaz, J. L. *et al.* Synthesis and biological evaluation of the 1-arylpyrazole class of σ1 receptor antagonists: Identification of 4-{2-[5-methyl-1- (naphthalen-2-yl)-1H-pyrazol-3-yloxy]ethyl}morpholine (S1RA, E-52862). *J. Med. Chem.* (2012). doi:10.1021/jm3007323

37. Torres, V. *et al.* QT prolongation and the antiarrhythmic efficacy of amiodarone. *J. Am.*

Coll. Cardiol. (1986). doi:10.1016/S0735-1097(86)80272-8

38. Vidal-Torres, A. *et al.* Effects of the selective sigma-1 receptor antagonist S1RA on formalin-induced pain behavior and neurotransmitter release in the spinal cord in rats. *J. Neurochem.* (2014). doi:10.1111/jnc.12648

39. Gris, G. *et al.* The selective sigma-1 receptor antagonist E-52862 attenuates neuropathic pain of different aetiology in rats. *Sci. Rep.* (2016). doi:10.1038/srep24591

40. Gordon, D. E. *et al.* A SARS-CoV-2 protein interaction map reveals targets for drug repurposing. *Nature* (2020). doi:10.1038/s41586-020-2286-9

41. Reghunathan, R. *et al.* Expression profile of immune response genes in patients with severe acute respiratory syndrome. *BMC Immunol.* (2005). doi:10.1186/1471-2172-6-2

42. Cutone, A. *et al.* Lactoferrin prevents LPS-induced decrease of the iron exporter ferroportin in human monocytes/macrophages. *BioMetals* (2014). doi:10.1007/s10534-014-9742-7

43. Conti, P. *et al.* Induction of pro-inflammatory cytokines (IL-1 and IL-6) and lung inflammation by COVID-19: anti-inflammatory strategies. *Journal of biological regulators and homeostatic agents* (2020). doi:10.23812/CONTI-E.

44. Lagunas-Rangel, F. A. & Chávez-Valencia, V. High IL-6/IFN-γ ratio could be associated with severe disease in COVID-19 patients. *Journal of Medical Virology* (2020). doi:10.1002/jmv.25900

45. Han, C. *et al.* Digestive Symptoms in COVID-19 Patients With Mild Disease Severity: Clinical Presentation, Stool Viral RNA Testing, and Outcomes. *Am. J. Gastroenterol.* (2020). doi:10.14309/ajg.0000000000000664

46. Oda, H. *et al.* Antiviral Effects of Bovine Lactoferrin on Human Norovirus. *Biochem. Cell Biol.* (2020). doi:10.1139/bcb-2020-0035

47. Mohamed, J. A. *et al.* A Novel Single-Nucleotide Polymorphism in the Lactoferrin Gene Is Associated with Susceptibility to Diarrhea in North American Travelers to Mexico. *Clin.*

Infect. Dis. (2007). doi:10.1086/512199

48. Gu, J., Han, B. & Wang, J. COVID-19: Gastrointestinal Manifestations and Potential Fecal–Oral Transmission. *Gastroenterology* (2020). doi:10.1053/j.gastro.2020.02.054

49. Hung, I. F.-N. *et al.* Triple combination of interferon beta-1b, lopinavir–ritonavir, and ribavirin in the treatment of patients admitted to hospital with COVID-19: an open-label, randomised, phase 2 trial. *Lancet* (2020). doi:10.1016/s0140-6736(20)31042-4

50. Berthold, M. R. *et al.* KNIME: The konstanz information miner. in *4th International Industrial Simulation Conference 2006, ISC 2006* (2006). doi:10.1145/1656274.1656280

51. Stevens, J.-L., Rudiger, P. & Bednar, J. HoloViews: Building Complex Visualizations Easily for Reproducible Science. in *Proceedings of the 14th Python in Science Conference* (2015). doi:10.25080/majora-7b98e3ed-00a